

Quenched nematic criticality and two superconducting domes in an iron-based superconductor

Pascal Reiss^{1*}, David Graf², Amir A. Haghimirad^{1,3}, William Knafo⁴, Loïc Drigo^{4,5}, Matthew Bristow¹, Andrew J. Schofield⁶ and Amalia I. Coldea^{1*}

The nematic electronic state and its associated critical fluctuations have emerged as a potential candidate for the superconducting pairing in various unconventional superconductors. However, in most materials their coexistence with magnetically ordered phases poses a significant challenge in determining their importance. Here, by combining chemical and hydrostatic physical pressure in $\text{FeSe}_{0.89}\text{S}_{0.11}$ we access a nematic quantum phase transition isolated from any other competing magnetic phases. From quantum oscillations in high magnetic fields, we trace the evolution of the Fermi surface and electronic correlations as a function of applied pressure and detect a Lifshitz transition that separates two distinct superconducting regions. One emerges from the nematic phase with a small Fermi surface and strong electronic correlations, while the other one has a large Fermi surface and weak correlations that promotes nesting and stabilization of a magnetically ordered phase at high pressures. The absence of mass divergence at the nematic quantum phase transition suggests that the nematic fluctuations could be quenched by the strong coupling to the lattice or local strain effects. A direct consequence is the weakening of superconductivity at the nematic quantum phase transition in the absence of magnetically driven fluctuations.

Quantum materials brought in the vicinity of a quantum critical point at absolute zero temperature have generated significant interest in condensed-matter physics as they can trigger the emergence of novel electronic states¹. In these extreme regimes, achieved by tuning external parameters, the nature of quasiparticles is significantly altered due to the interactions with critical fluctuations and non-Fermi liquid behaviour is often observed². A particularly interesting instability of a metallic system is the electronic nematic state. In such a state, the electron motion spontaneously breaks the rotational symmetry of the crystal in the presence of strong electronic interactions and its Fermi surface undergoes a spontaneous distortion³. The observation of electronic nematic order in different families of high-temperature superconductors implies that the same interactions may be involved in stabilizing both the nematic and superconducting states^{4–6}. However, the presence of other competing electronic phases, such as spin or charge-density waves, can obscure the relevance of the nematic fluctuations in superconducting pairing.

FeSe is an example of a nematic superconductor in which applied pressure leads to a fourfold increase in its bulk superconductivity (from 9 K towards a high critical temperature, $T_c \approx 40$ K)^{7,8}. In the normal state, the nematic phase transition of FeSe is suppressed with increasing pressure, but the quantum phase transition is masked by an emerging magnetic ordering stabilized under high pressures^{9–16}. As the nematic and magnetic phases of FeSe are intertwined, it is difficult to establish the roles played by nematic or spin fluctuations for stabilizing the high- T_c state. Similarly, isostructural sulfur substitution in $\text{FeSe}_{1-x}\text{S}_x$, equivalent to internal positive pressure,

suppresses the nematic order, but does not stabilize a magnetically ordered state^{17–21}. Consequently, by combining chemical pressure and hydrostatic pressure, a nematic quantum critical point can be unmasked, as the magnetic order is shifted to higher pressures with increasing sulfur concentration^{21–24}. This opens a unique path for studying the nature of nematic criticality using hydrostatic pressure as a clean tuning parameter and to probe the role of nematic fluctuations in stabilizing superconductivity.

As superconductivity depends not only on the origin of the attractive pairing interaction but also on the details of the Fermi surface²⁵, understanding the changes in the electronic structure as a function of different tuning parameters is paramount. Furthermore, the size of the Fermi energy can trigger different electronic instabilities: a nematic order for small energies, superconductivity in an intermediate regime or a magnetically ordered state for large energies²⁶. To test these different regimes, quantum oscillations are a powerful technique to access the evolution of the electronic structure and correlations under extreme conditions.

Here, we explore the electronic behaviour across the pressure–temperature phase diagram of $\text{FeSe}_{0.89}\text{S}_{0.11}$, in the absence of long-range magnetic order. Using external pressure, we finely tune the system across its nematic phase transition to understand the nature of the critical regime and to establish the role played by the electronic correlations, electronic structure and scattering in stabilizing superconductivity. We identify an extended region with a $\sim T^{3/2}$ resistivity that evolves into a Fermi liquid behaviour at low temperatures in the vicinity of the nematic phase transition. We find that the cyclotron effective masses from quantum oscillations are

¹Clarendon Laboratory, Department of Physics, University of Oxford, Oxford, UK. ²National High Magnetic Field Laboratory, Florida State University, Tallahassee, FL, USA. ³Institut für Festkörperphysik, Karlsruhe Institute of Technology, Karlsruhe, Germany. ⁴Laboratoire National des Champs Magnétiques Intenses, UPR 3228, CNRS-UJF-UPS-INSA, Toulouse, France. ⁵Geosciences Environment Toulouse - GET UMR5563 CNRS, UR234 IRD, UPS, CNES, Toulouse, France. ⁶School of Physics and Astronomy, University of Birmingham, Edgbaston, UK. *e-mail: pascal.reiss@physics.ox.ac.uk; amalia.coldea@physics.ox.ac.uk

significantly suppressed across the nematic phase transition, as is superconductivity. This behaviour could be a signature of quenched critical fluctuations due to a nematoelastic coupling to the lattice²⁷, and/or local strain effects.

Temperature dependence of resistivity with pressure

Figure 1a shows the evolution of the temperature dependence of the resistivity as a function of applied pressure below 100 K (the full range up to 300 K is shown in Supplementary Fig. 1). With increasing pressure, the nematic transition temperature T_s is quickly suppressed from 60 K at ambient pressure until it becomes unobservable around p_c (Supplementary Fig. 1) and no hysteresis between warming and cooling at constant pressure is detected (see Supplementary Fig. 9). By extrapolating the pressure evolution of T_s to zero, we can locate the position of the nematic quantum phase transition at $p_c \approx 5.8(5)$ kbar in Fig. 1e. Within the nematic phase, there is only a weak pressure dependence of the superconducting transition temperature T_c (defined as the zero-resistivity temperature), similar to previous findings using chemical pressure^{19,20}. Outside the nematic phase, superconductivity is suppressed rather than enhanced in the proximity of the nematic quantum phase transition and reaches a minimum $T_c \approx 6.4$ K (at ≈ 7 kbar) close to p_c . However, superconductivity is enhanced significantly towards 22 K at 20 kbar, and T_c was reported to reach 30 K at higher pressures at around 30 kbar (ref. ²²). The superconducting transition at high pressures broadens significantly compared with the low-pressure region (by a factor ≈ 10), suggesting that the superconducting phase becomes rather inhomogeneous at high pressures or that it coexists with another electronic phase. In contrast to FeSe where nematicity, magnetism and superconductivity may coexist under pressure^{9,13,23}, magnetic order in our composition is expected to be stabilized only at high pressures exceeding 40 kbar (ref. ²²).

To elucidate the nature of quasiparticle scattering in the proximity of the nematic quantum phase transition, we investigate the resistivity exponent n , defined as $\rho(T) = \rho_0 + AT^n$, as a function of pressure and temperature. For a non- or weakly interacting Fermi liquid, one expects $n=2$. In contrast, for systems in the proximity of quantum critical points, enhanced order parameter fluctuations can lead to non-Fermi liquid behaviour with an exponent $n < 2$ and additional scattering^{5,28,29}. The precise power law is influenced by the nature of the critical fluctuations (their wavevector and dynamical exponent), by dimensionality³⁰, by the amount of disorder²⁸ and by nearby quantum critical points³¹. The nematic critical fluctuations can be exceedingly effective in destroying quasiparticles and can produce a striking nodal–antinodal dichotomy generating non-Fermi liquid-like behaviour over much of the Fermi surface, enhancing resistivity^{5,32}. At low temperatures away from the critical points in a clean system, Fermi-liquid-like behaviour is often recovered^{30,33}. In this regime, the A coefficient, which is a measure of the strength of the electronic correlations as $A \sim (m^*/m_e)^2$, diverges on approaching the critical region as fluctuations become critical (m^* is the quasiparticle effective mass)^{34,35}.

Figure 1e shows the temperature and pressure dependence of n as a colour map. Near the nematic end point at p_c , the resistivity does not follow a linear T dependence, as found near magnetic critical points³⁴, nor does it display the expected quantum critical fan with a constant exponent³⁰. Instead, this region is best represented by a temperature-dependent resistivity exponent n , shown in Fig. 1b, that evolves from a value around $n=3/2$ at high temperatures towards the $n=2$ value in the low-temperature regime. In fact, n shows a marked upturn below 30 K for pressures close to p_c that can be linearly extrapolated towards $n=2$, as shown by the dashed lines in Fig. 1b. To further demonstrate this result, we can use magnetic fields to suppress superconductivity. At the lowest temperatures below 15 K, we find a Fermi-liquid behaviour for all pressures across p_c , as shown in Fig. 1d (see also Supplementary Figs. 1 and 3).

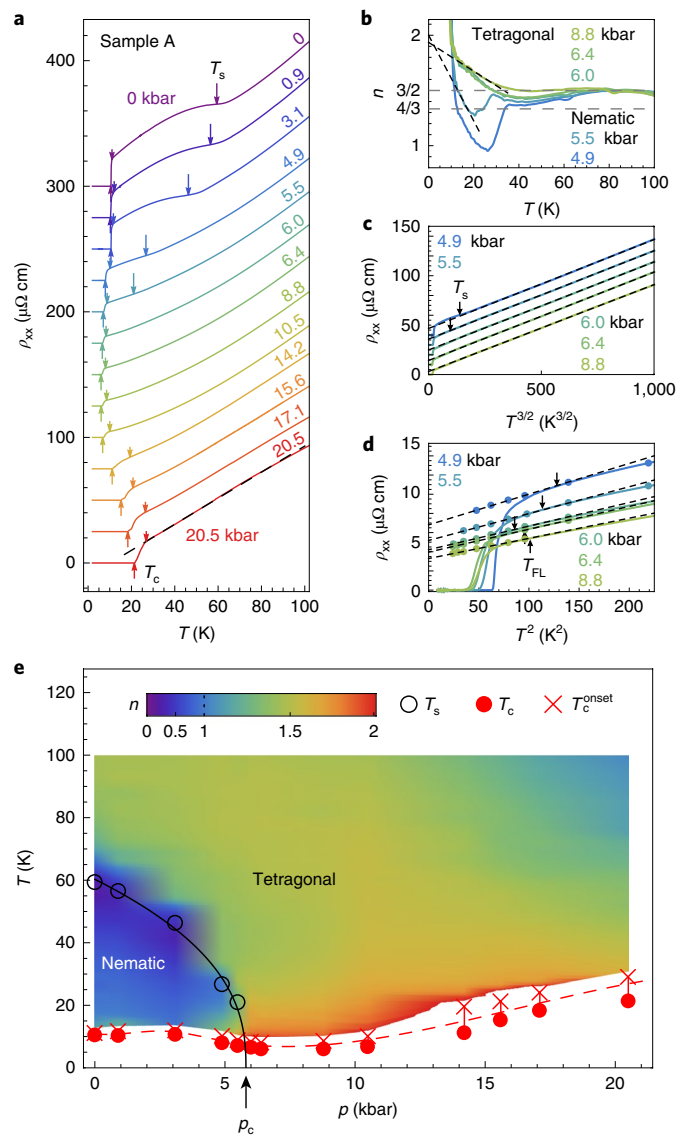


Fig. 1 | Transport under pressure in $\text{FeSe}_{0.89}\text{S}_{0.11}$. **a**, The temperature dependence of the resistivity for different pressures. The transition temperature into the nematic state occurs at T_s and into the superconducting phase at T_c . The onset and offset of superconductivity are indicated by crosses and solid circles, respectively in **e**. **b**, The local resistivity exponent n for pressures close to p_c . The dashed lines are linear fits at low temperatures above the onset of superconductivity. **c**, High-temperature resistivity plotted against $T^{3/2}$. The dashed lines are linear fits. The data in **a** and **c** are shifted vertically for clarity. **d**, Low-temperature resistivity (solid lines) and normal-state resistivity extrapolated from symmetrized magnetic field measurements (points) plotted against T^2 (Supplementary Fig. 2). The dashed lines are fits to Fermi liquid behaviour, $\rho = \rho_0 + AT^2$, the slope gives the A coefficient and ρ_0 is the zero-temperature residual resistivity. Fit residuals are shown in Supplementary Fig. 3. **e**, The pressure–temperature phase diagram. The colour map represents the local resistivity exponent n ($\rho \propto T^n$); see the colour scale in the inset. The symbols indicate the transition temperatures defined in **a**. The dashed line is a guide to the eye. The solid line is a fit of $T_s \propto (p - p_c)^\epsilon$ giving $\epsilon \approx 0.4(1)$ and $p_c = 5.8(5)$ kbar. To establish the value of the critical exponent, detailed pressure points close to p_c are required, as detailed in ref. ⁵¹.

Furthermore, the corresponding A coefficient and the zero-temperature resistivity, ρ_0 , are continuously suppressed with increasing pressure across the transition (Fig. 4b and Supplementary Fig. 1).

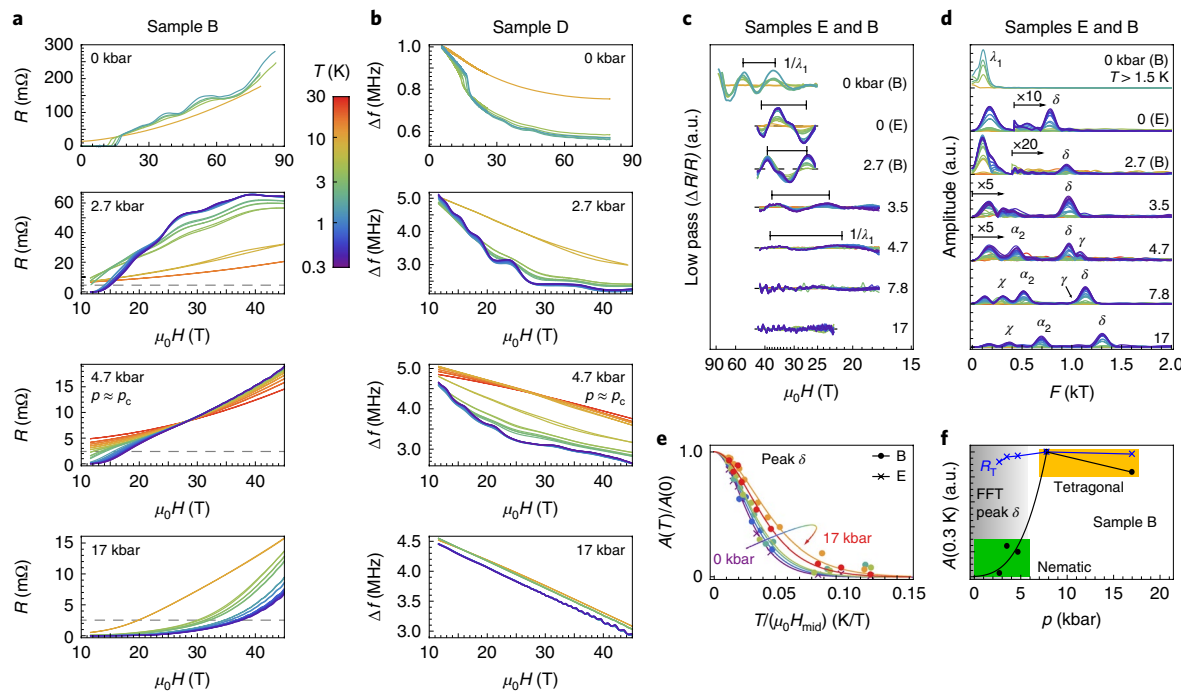


Fig. 2 | Evolution of quantum oscillations with pressure in $\text{FeSe}_{0.89}\text{S}_{0.11}$. **a,b**, Magnetotransport (**a**) and TDO resonant frequency variation, Δf (MHz) (**b**), for several different samples as a function of applied pressure (see also Supplementary Figs. 4–6). The horizontal dashed lines in **a** indicate the sample resistance in zero field at the onset of superconductivity. **c**, The oscillatory component of the magnetoresistance (after subtracting a smooth background with a low-pass filter applied) shows the evolution of the dominant low-frequency oscillation. The dashed lines here indicate the base line. The horizontal bars indicate the period of the dominant low frequency (λ_1). **d**, Fourier transform of the oscillatory part of the magnetotransport data in **a** after the background subtraction. The distinct peaks identified correspond to extremal cross-sections of the Fermi surface. **e**, The temperature dependence of the amplitude gives the cyclotron effective band mass of the δ orbit for different pressures. The lines are fits to the Lifshitz-Kosevich mass damping term³⁹. **f**, Low-temperature amplitude variation with pressure of the δ orbit (solid symbols) and the expected amplitude variation due to the mass damping term R_T (cross symbols). The solid lines are guides to the eye. FFT, fast Fourier transform. The data in **c** and **d** are shifted vertically for clarity.

This strongly suggests that at p_c the nematic fluctuations do not become critical.

The evolution of the Fermi surface with pressure

Next, we use quantum oscillation measurements under pressure to follow the evolution of the Fermi surface and to assess the strength of electronic correlations across the phase diagram of $\text{FeSe}_{0.89}\text{S}_{0.11}$ under pressure. Figure 2a,b shows the field dependence of the resistance and tunnel diode oscillator (TDO) data for pressures up to 17 kbar and up to 45 T, and the ambient pressure measurements up to 80 T for three different samples. Results on additional samples and pressures are shown in Supplementary Figs. 4–8. There are different field regimes seen in the raw data: the superconducting state with zero resistance at low magnetic fields; finite resistance that increases strongly with magnetic field in the crossover vortex-liquid region to the normal state at higher fields; and normal magnetoresistance accompanied by quantum oscillations in high magnetic fields.

At low pressures in the nematic state, the magnetotransport and TDO data are dominated by a low-frequency oscillation (Fig. 2a) that disappears beyond 4.7 kbar, in the proximity of p_c (Fig. 2a–c). At high pressures and in high fields, a high-frequency oscillation is visible in the raw data (see Fig. 2a,b), associated with a large Fermi surface sheet. This rules out a reconstruction of the Fermi surface at high pressures, outside the nematic phase, similar to the tetragonal phases of $\text{FeSe}_{1-x}\text{S}_x$ (ref. ¹⁹), but in contrast to FeSe under pressure inside the magnetic phase¹⁰.

Quantum oscillation spectra of $\text{FeSe}_{0.89}\text{S}_{0.11}$ reveal several distinct peaks, consistent with a complex multiband electronic structure, as shown in Fig. 2d. On the basis of angle-resolved photoemission

spectroscopy (ARPES) data and previous quantum oscillation measurements, the ambient-pressure Fermi surface is formed of two concentric electron-like and one outer hole-like quasi-two-dimensional (2D) sheets (containing the β and δ orbits) as well as a small inner 3D hole pocket centred at the Z-point (γ), shown in Fig. 3d^{18,20,25}. As a function of applied pressure, the cylindrical Fermi surfaces can become warped along the k_z direction, either due to changes in the degree of interlayer hopping and/or electronic correlations. These effects can trigger a Lifshitz transition and the disappearance of the neck orbits (such as β or α_1 in Fig. 3d), as found in $\text{FeSe}_{1-x}\text{S}_x$ (ref. ¹⁹). The multiband structure of $\text{FeSe}_{0.89}\text{S}_{0.11}$ could give rise to up to a maximum of seven frequencies, not all of which can be identified in experiment. The high-pressure region is dominated by the largest orbit of the hole band, δ , as shown in Fig. 2d (see also ref. ³⁶). Weaker features associated with the largest orbit of the electron band, γ , can be also detected at some pressures and in the TDO signal, as shown in Supplementary Fig. 7.

With increasing pressure, all frequencies increase in size, with the exception of the lowest two frequencies, as summarized in Fig. 3a. At the highest pressure, the Fermi surface area of the δ pocket has expanded almost by a factor two, as compared with its size at ambient pressure. This is much more than the expected growth of the Brillouin zone (less than 4%), assuming a simple contraction of the in-plane unit cell^{14,37}. On the other hand, the dominant low frequency, λ_1 (in Fig. 2c and Supplementary Figs. 4–6), disappears together with nematicity close to p_c (see λ_1 in Fig. 3a). We attribute the loss of this frequency to a Lifshitz transition that can be triggered by changes in the interlayer coupling tuned by pressure. This observation is in agreement with the topological change of

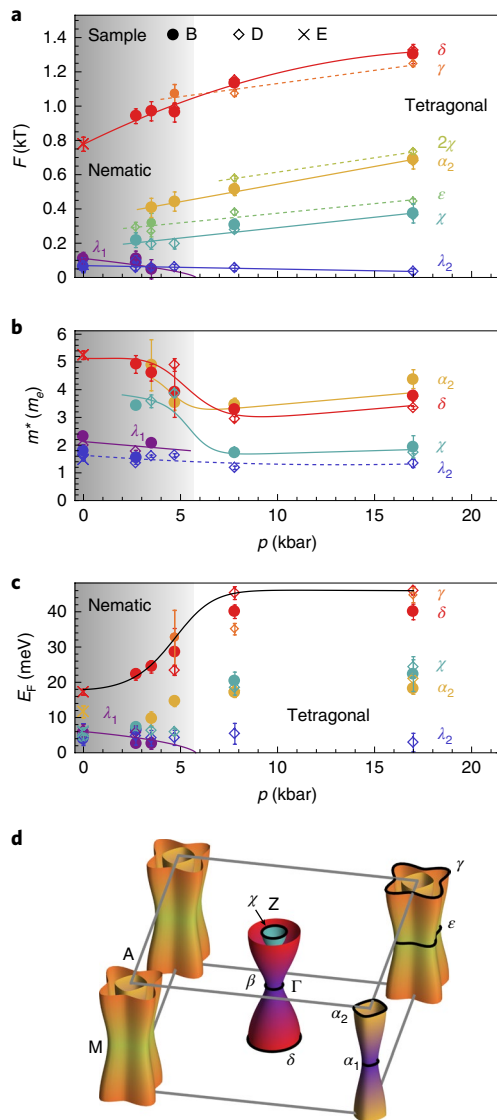


Fig. 3 | Pressure tuning of Fermi surface and electronic correlations. **a,b**, Quantum oscillation frequencies (**a**) and the cyclotron masses (**b**) as a function of pressure for samples B, D and E. The masses associated with χ and δ orbits show a clear decrease on crossing the nematic phase transition. A topological Lifshitz transition occurs at p_c and one small orbit in the $k_z=0$ plane disappears (either β or α_1 can be assigned to λ_1). A small frequency λ_2 is detected only in TDO and it seems weakly affected by pressure. **c**, The Fermi energy E_F assuming parabolic band dispersions, based on Fermi surface cross-sections and quasiparticle masses (**a** and **b**). The lines are guides to the eye. The splitting of the γ and δ frequencies is summarized in Supplementary Fig. 7. The shaded areas indicate the nematic phase. **d**, A sketch of the Fermi surface in the nematic phase and the different 2D orbits, based on ARPES and quantum oscillation measurements^{18–20}. The error bars correspond to a 1σ confidence interval.

the Fermi surface using sulfur substitution, equivalent to positive pressure¹⁹. The presence of small pockets with Fermi energies of the order 3–5 meV in Fig. 3c, comparable to the superconducting gap (Supplementary Fig. 6), creates conditions for a Bardeen–Cooper–Schrieffer to Bose–Einstein condensation crossover³⁸.

Quasiparticle masses

We now turn to the evolution of the electronic correlations across the phase diagram. The evolution of the cyclotron effective mass,

m^* , is extracted from the temperature dependence of the quantum oscillation amplitudes, analysed quantitatively within the Lifshitz–Kosevich formalism (Fig. 2e)³⁹, and summarized in Fig. 3b. The quasiparticle masses of the δ orbit can be extracted across the entire pressure range, as shown in Fig. 2e, and their amplitudes show an unusual pressure dependence in Fig. 2f. The cyclotron mass of the largest frequency, δ (as well as χ and γ in Supplementary Fig. 7), decreases significantly with increasing pressure from $5 m_e$ to $3 m_e$, signifying a strong reduction in electronic correlations away from the nematic phase transition. Thus, the quasiparticle masses gradually decrease rather than showing a divergent behaviour across the nematic end point around p_c . In the high-pressure regime, a slight increase in the effective masses of the δ and χ orbits is observed, but their values remain smaller than in the nematic phase, despite the fact that superconductivity has increased twice. Furthermore, the masses associated with the γ orbit, expected to contain d_{xy} orbital character, are much heavier than those associated with the δ orbit in FeSe (refs. ^{17,25,40}), but they cannot be clearly distinguished across the entire pressure phase diagram (as shown in Supplementary Fig. 7). However, the role of orbital-dependent electronic correlations cannot be fully assessed as the quasiparticle masses in quantum oscillations contain information about the cyclotron orbits that have averaged orbital character.

Discussion

The superconducting phase of $\text{FeSe}_{0.89}\text{S}_{0.11}$ under pressure is composed of two distinct superconducting domes, separated by a Lifshitz transition. The first one at low pressure emerges from the nematic phase (SC1 in Fig. 4b) and the second one at high pressure approaching the spin-density wave phase (SC2 in Fig. 4a,b). The two domes can also be visualized in the pressure–temperature phase diagram in magnetic fields of 8 T in Fig. 4b. Remarkably, the nematic quantum phase transition is located in the normal state between the two superconducting domes. Different types of superconducting pairing inside and outside the nematic phase were suggested to occur in $\text{FeSe}_{1-x}\text{S}_x$, on the basis of scanning tunnelling microscopy, specific heat and thermal conductivity studies^{41,42}.

The cyclotron effective masses, which measure the strength of electronic correlations, vary with pressure, being in general larger inside the nematic phase compared with those in the tetragonal phase. Interestingly, we find a qualitative link between the cyclotron masses of the δ orbit, the A coefficient from the low-temperature resistivity data, and the value of T_c in the nematic phase and in the low- T_c tetragonal phase, as shown in Fig. 4b. This suggests that the hole bands are closely involved in the pairing mechanism. This correlation between the band renormalization and T_c was also captured by quantum oscillation experiments and ARPES studies on $\text{FeSe}_{1-x}\text{S}_x$ (refs. ^{19,20}). Furthermore, NMR studies show that the strength of antiferromagnetic fluctuations also correlates with T_c within the nematic phase, being suppressed together with the nematicity^{43,44}. Here, for higher pressures, the correlation between the hole-like band masses and T_c is lost, suggesting changes in the pairing mechanism towards the high- T_c phase. Furthermore, the observed Lifshitz transition of one of the pockets could also affect T_c as it causes the density of states available for pairing to decrease. This decrease is likely to be weak and it is compensated by the contributions from other quasi-2D Fermi surfaces that grow with pressure.

On approaching a critical region as a function of the tuning parameter, the quasiparticle masses m^* (ref. ⁴⁵) and the A transport coefficient should diverge and the superconductivity should be enhanced^{30,35,45}. Here, near the nematic end point at p_c in the absence of magnetic order, we find a smoothly evolving A coefficient and effective masses for the large, well-defined orbit (δ) in Fig. 4b. This suggests that the nematic fluctuations are finite and not critical at p_c . Additionally, the superconducting transition temperature is minimal in the vicinity of the nematic quantum phase

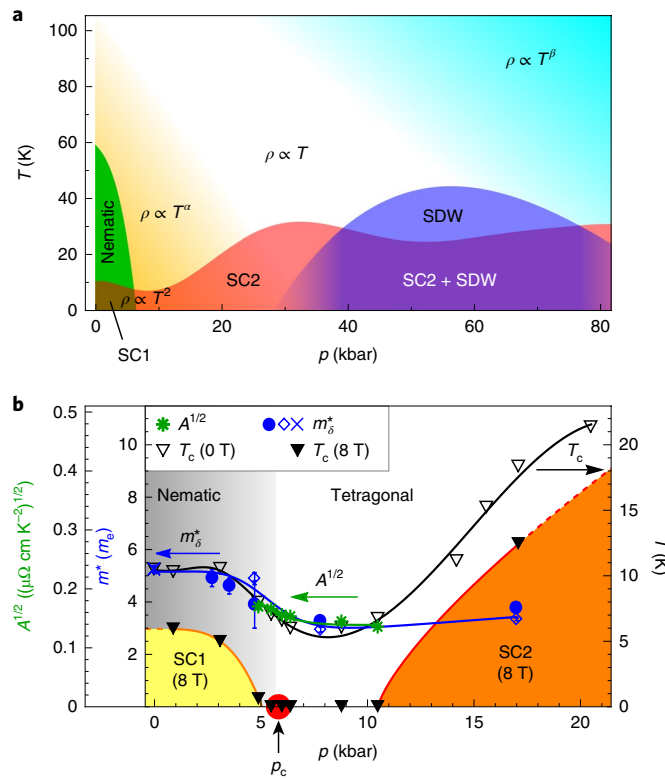


Fig. 4 | Pressure-temperature phase diagrams. **a**, An extended phase diagram of $\text{FeSe}_{0.89}\text{S}_{0.11}$ based on our work and previous reports²². **b**, Comparison of the band masses of the δ orbit with T_c and the Fermi liquid coefficient, A . There is a qualitative link between the pressure dependence of electronic correlations and superconductivity across the nematic phase transition, which is lost towards the high-pressure high- T_c state. The temperature-pressure phase diagram in a static magnetic field of 8 T shows the separation of the two superconducting domes unmasking the nematic quantum phase transition at p_c . The symbols for the masses of the δ orbits are identical to those in Fig. 3. The solid lines are guides to the eye and the dashed lines are extrapolations. The error bars correspond to a 1σ confidence interval.

transition at p_c . This implies that the suppression of superconductivity is connected with the lack of nematic critical fluctuations and/or spin fluctuations in this regime. Collapse of critical nematic fluctuations was observed in Raman measurements in FeSe under pressure, indicating that they play a marginal role in stabilizing superconductivity⁴⁶. This is in contrast to other iron-based superconductors where critical nematic and/or magnetic fluctuations enhance superconductivity approaching a spin-density wave state^{5,34}.

The absence of divergent critical nematic fluctuations could suggest the presence of a coupling of the nematic order parameter with the shear mode of the lattice leading to quenched nematic criticality along certain directions^{27,47}. This coupling could suppress superconductivity⁴⁷ and lead to a finite quasiparticle mass in the proximity of the putative nematic quantum critical point (compared with data in Supplementary Fig. 7). One test of this model is the predicted crossover from non-Fermi liquid behaviour at high temperatures towards a Fermi liquid at low temperatures, below T_{FL} . We can estimate that for our system $T_{FL} \approx 13$ K, which is in good agreement with the extracted values from our transport experiments ($T_{FL} \approx 9$ –11 K, as indicated by the arrows in Fig. 1d and detailed in the Methods). Furthermore, the resistivity exponent n close to p_c in our study is not constant and it has a strong temperature dependence (Fig. 1b), as predicted for transport due to the coupling with the lattice via

acoustic phonons⁴⁸. Similar transport behaviour and power laws reported here for $\text{FeSe}_{0.89}\text{S}_{0.11}$ in the vicinity of the nematic end point were also found in $\text{FeSe}_{1-x}\text{S}_x$ (ref. ⁴⁹). In any case, the transport behaviour near a nematic end point is very different from the linear T behaviour in the proximity of a magnetic quantum critical point³⁴.

Additionally, the substitutional disorder of sulfur for selenium outside the Fe planes can lead to local strain that can potentially affect the nematic order parameter, acting as local fields and providing the realization of the random Ising model⁵⁰. In this scenario, the induced local strains can set a limit of the correlation lengths and hence affect the nature of the nematic phase transition at low temperatures. While inherent substitutional disorder exists at ambient pressure (setting up the limit on the mean free path of ≈ 350 Å, as shown in Supplementary Fig. 8), the amount of disorder is a constant across the pressure-tuned nematic phase transition. Future theoretical models need to address how local strain (by scanning tunnelling microscopy as in ref. ⁴¹) combined with applied pressure affects critical behaviour in these types of system. This approach could also provide insight into the significant suppression of the amplitude of the quantum oscillation of the δ orbit inside the nematic phase beyond the normal damping terms due to disorder or the change in masses, as shown in Fig. 2f. Last, the nematic phase transition and the Lifshitz transition seem to coincide both with applied and chemical pressure¹⁹. The collapse of the critical nematic fluctuations and phonon anomalies were directly linked to the change in topology of the Fermi surface of FeSe under pressure from Raman studies⁴⁶.

The electronic signature of the nematic end point is substantially different from other critical points in iron-based superconductors, where both magnetic and nematic phases closely coexist and superconductivity is enhanced. The absence of divergent electronic correlations at the nematic phase transition invokes a coupling of the electronic system with the local environment. However, these effects are detrimental for supporting a high- T_c phase, and consequently the pairing mechanism is weakened where spin fluctuations are absent.

Online content

Any methods, additional references, Nature Research reporting summaries, source data, statements of code and data availability and associated accession codes are available at <https://doi.org/10.1038/s41567-019-0694-2>.

Received: 1 November 2018; Accepted: 17 September 2019;

Published online: 28 October 2019

References

- Sachdev, S. & Keimer, B. Quantum criticality. *Phys. Today* **64**, 29–35 (2011).
- Schofield, A. J. Non-Fermi liquids. *Contemp. Phys.* **40**, 95–115 (1999).
- Pomeranchuk, I. I. On the stability of a Fermi liquid. *Phys. Rev. Lett.* **8**, 361 (1958).
- Fernandes, R. M., Chubukov, A. V. & Schmalian, J. What drives nematic order in iron-based superconductors? *Nat. Phys.* **10**, 97–104 (2014).
- Lederer, S., Schattner, Y., Berg, E. & Kivelson, S. Superconductivity and non-Fermi liquid behavior near a nematic quantum critical point. *Proc. Natl Acad. Sci. USA* **114**, 4905–4910 (2017).
- Sprau, P. O. et al. Discovery of orbital-selective Cooper pairing in FeSe. *Science* **357**, 75–80 (2016).
- Mizuguchi, Y., Tomioka, F., Tsuda, S., Yamaguchi, T. & Takano, Y. Superconductivity at 27 K in tetragonal FeSe under high pressure. *Appl. Phys. Lett.* **93**, 152505 (2008).
- Medvedev, S. et al. Electronic and magnetic phase diagram of $\beta\text{-Fe}_{1.01}\text{Se}$ with superconductivity at 36.7 K under pressure. *Nat. Mater.* **8**, 630–633 (2009).
- Terashima, T. et al. Pressure-induced antiferromagnetic transition and phase diagram in FeSe. *J. Phys. Soc. Jpn* **84**, 063701 (2015).
- Terashima, T. et al. Fermi surface reconstruction in FeSe under high pressure. *Phys. Rev. B* **93**, 094505 (2016).
- Wang, F., Kivelson, S. A. & Lee, D.-H. Nematicity and quantum paramagnetism in FeSe. *Nat. Phys.* **11**, 959–963 (2015).
- Wang, Q. et al. Strong interplay between stripe spin fluctuations, nematicity and superconductivity in FeSe. *Nat. Mater.* **15**, 159–163 (2016).

13. Sun, J. P. et al. High- T_c superconductivity in FeSe at high pressure: dominant hole carriers and enhanced spin fluctuations. *Phys. Rev. Lett.* **118**, 147004 (2017).
14. Kothapalli, K. et al. Strong cooperative coupling of pressure-induced magnetic order and nematicity in FeSe. *Nat. Commun.* **7**, 12728 (2016).
15. Imai, T., Ahilan, K., Ning, F. L., McQueen, T. M. & Cava, R. J. Why does undoped FeSe become a high- T_c superconductor under pressure? *Phys. Rev. Lett.* **102**, 177005 (2009).
16. Bendele, M. et al. Pressure induced static magnetic order in superconducting FeSe_{1-x}. *Phys. Rev. Lett.* **104**, 087003 (2010).
17. Watson, M. D. et al. Emergence of the nematic electronic state in FeSe. *Phys. Rev. B* **91**, 155106 (2015).
18. Watson, M. D. et al. Suppression of orbital ordering by chemical pressure in FeSe_{1-x}S_x. *Phys. Rev. B* **92**, 121108 (2015).
19. Coldea, A. I. et al. Evolution of the low-temperature Fermi surface of superconducting FeSe_{1-x}S_x across a nematic phase transition. *npj Quantum Mater.* **4**, 2 (2019).
20. Reiss, P. et al. Suppression of electronic correlations by chemical pressure from FeSe to FeS. *Phys. Rev. B* **96**, 121103 (2017).
21. Hosoi, S. et al. Nematic quantum critical point without magnetism in FeSe_{1-x}S_x superconductors. *Proc. Natl Acad. Sci. USA* **113**, 8139–8143 (2016).
22. Matsuura, K. et al. Maximizing T_c by tuning nematicity and magnetism in FeSe_{1-x}S_x superconductors. *Nat. Commun.* **8**, 1143 (2017).
23. Xiang, L. et al. Dome of magnetic order inside the nematic phase of sulfur-substituted FeSe under pressure. *Phys. Rev. B* **96**, 024511 (2017).
24. Yip, K. Y. et al. Weakening of the diamagnetic shielding in FeSe_{1-x}S_x at high pressures. *Phys. Rev. B* **96**, 020502 (2017).
25. Coldea, A. I. & Watson, M. D. The key ingredients of the electronic structure of FeSe. *Annu. Rev. Cond. Matt. Phys.* **9**, 125–146 (2018).
26. Chubukov, A. V., Khodas, M. & Fernandes, R. M. Magnetism, superconductivity, and spontaneous orbital order in iron-based superconductors: which comes first and why? *Phys. Rev. X* **6**, 041045 (2016).
27. Paul, I. & Garst, M. Lattice effects on nematic quantum criticality in metals. *Phys. Rev. Lett.* **118**, 227601 (2017).
28. Rosch, A. Interplay of disorder and spin fluctuations in the resistivity near a quantum critical point. *Phys. Rev. Lett.* **82**, 4280–4283 (1999).
29. Maslov, D. L., Yudson, V. I. & Chubukov, A. V. Resistivity of a non-Galilean-invariant Fermi liquid near Pomeranchuk quantum criticality. *Phys. Rev. Lett.* **106**, 106403 (2011).
30. Löhlneysen, Hv, Rosch, A., Vojta, M. & Wölfle, P. Fermi-liquid instabilities at magnetic quantum phase transitions. *Rev. Mod. Phys.* **79**, 1015–1075 (2007).
31. Oliver, G. T. *Quantum Multicriticality*. PhD thesis, Univ. Birmingham (2017).
32. Wang, X. & Berg, E. Scattering mechanisms and electrical transport near an Ising nematic quantum critical point. *Phys. Rev. B* **99**, 235136 (2019).
33. Licciardello, S. et al. Electrical resistivity across a nematic quantum critical point. *Nature* **567**, 213–217 (2019).
34. Kasahara, S. et al. Evolution from non-Fermi- to Fermi-liquid transport via isovalent doping in BaFe₂(As_{1-x}P_x)₂ superconductors. *Phys. Rev. B* **81**, 184519 (2010).
35. Analytis, J. G. et al. Transport near a quantum critical point in BaFe₂(As_{1-x}P_x)₂. *Nat. Phys.* **10**, 194–197 (2014).
36. Watson, M. D. et al. Dichotomy between the hole and electron behavior in multiband superconductor FeSe probed by ultrahigh magnetic fields. *Phys. Rev. Lett.* **115**, 027006 (2015).
37. Tomita, T. et al. Correlation between T_c and crystal structure in S-doped FeSe superconductors under pressure: studied by x-ray diffraction of FeSe_{0.8}S_{0.2} at low temperatures. *J. Phys. Soc. Jpn.* **84**, 1–8 (2015).
38. Kasahara, S. et al. Field-induced superconducting phase of FeSe in the BCS–BEC cross-over. *Proc. Natl Acad. Sci. USA* **111**, 16309–16313 (2014).
39. Shoenberg, D. *Magnetic Oscillations in Metals* (Cambridge Univ. Press, Cambridge, 1984).
40. Terashima, T. et al. Anomalous Fermi surface in FeSe seen by Shubnikov–de Haas oscillation measurements. *Phys. Rev. B* **90**, 144517 (2014).
41. Hanaguri, T. et al. Two distinct superconducting pairing states divided by the nematic end point in FeSe_{1-x}S_x. *Sci. Adv.* **4**, eaar6419 (2018).
42. Sato, Y. et al. Abrupt change of the superconducting gap structure at the nematic critical point in FeSe_{1-x}S_x. *Proc. Natl Acad. Sci. USA* **115**, 1227–1231 (2018).
43. Kuwayama, T. et al. ⁷⁷Se-NMR study under pressure on 12%-S doped FeSe. *J. Phys. Soc. Jpn.* **88**, 033703 (2019).
44. Wiecki, P. et al. Persistent correlation between superconductivity and antiferromagnetic fluctuations near a nematic quantum critical point in FeSe_{1-x}S_x. *Phys. Rev. B* **98**, 020507 (2018).
45. Shishido, H. et al. Evolution of the Fermi surface of BaFe₂(As_{1-x}P_x)₂ on entering the superconducting dome. *Phys. Rev. Lett.* **104**, 057008 (2010).
46. Massat, P. et al. Collapse of critical nematic fluctuations in FeSe under pressure. *Phys. Rev. Lett.* **121**, 077001 (2018).
47. Labat, D. & Paul, I. Pairing instability near a lattice-influenced nematic quantum critical point. *Phys. Rev. B* **96**, 195146 (2017).
48. de Carvalho, V. S. & Fernandes, R. M. Resistivity near a nematic quantum critical point: impact of acoustic phonons. *Phys. Rev. B* **100**, 115103 (2019).
49. Bristow, M. et al. Anomalous high-magnetic field electronic state of the nematic superconductors FeSe_{1-x}S_x. Preprint at <https://arXiv.org/abs/1904.02522> (2019).
50. Carlson, E. W., Dahmen, K. A., Fradkin, E. & Kivelson, S. A. Hysteresis and noise from electronic nematicity in high-temperature superconductors. *Phys. Rev. Lett.* **96**, 097003 (2006).
51. Jaramillo, R., Feng, Y., Wang, J. & Rosenbaum, T. F. Signatures of quantum criticality in pure Cr at high pressure. *Proc. Natl Acad. Sci. USA* **107**, 13631–13635 (2010).

Acknowledgements

We thank P. Cai for technical support with setting up the Physical Property Measurement System pressure cell and A. Chubukov, E. Berg, R. Fernandes, I. Paul, R. Valenti, I. Vekhter, M. Watson, Z. Zajicek, S. Parameswaran and S. Simon for useful discussions and comments. This work was mainly supported by the EPSRC (EP/I004475/1, EP/I017836/1). A.A.H. acknowledges the financial support of the Oxford Quantum Materials Platform Grant (EP/M020517/1). A portion of this work was performed at the National High Magnetic Field Laboratory, which is supported by National Science Foundation Cooperative Agreement No. DMR-1157490 and the State of Florida. Part of this work was supported by HFML-RU/FOM and LNCMI-CNRS, members of the European Magnetic Field Laboratory (EMFL) and by EPSRC (UK) via its membership to the EMFL (grant no. EP/N01085X/1). Part of this work at the LNCMI was supported by Programme Investissements d'Avenir under the programme ANR-11-IDEX-0002-02, reference ANR-10-LABX-0037-NEXT. A.I.C. acknowledges the hospitality of KITP supported by the National Science Foundation under grant no. NSF PHY-1125915. We also acknowledge financial support of the John Fell Fund of Oxford University. A.I.C. acknowledges an EPSRC Career Acceleration Fellowship (EP/I004475/1) and Oxford Centre for Applied Superconductivity.

Author contributions

A.I.C. proposed and supervised the project. P.R., D.G. and A.I.C. performed experiments in the hybrid magnet in Tallahassee. P.R., W.K., L.D., M.B. and A.I.C. performed experiments in pulsed fields in Toulouse. A.A.H. grew the single crystals. A.J.S. provided theoretical input. P.R. and A.I.C. performed data analysis and wrote the paper with contributions and comments from all of the authors.

Competing interests

The authors declare no competing interests.

Additional information

Supplementary information is available for this paper at <https://doi.org/10.1038/s41567-019-0694-2>.

Correspondence and requests for materials should be addressed to P.R. or A.I.C.

Peer review information *Nature Physics* thanks Yann Gallais, Maxim Khodas, Liling Sun and the other, anonymous, reviewer(s) for their contribution to the peer review of this work.

Reprints and permissions information is available at www.nature.com/reprints.

Publisher's note Springer Nature remains neutral with regard to jurisdictional claims in published maps and institutional affiliations.

© The Author(s), under exclusive licence to Springer Nature Limited 2019

Methods

Sample characterization. Single crystals of $\text{FeSe}_{0.89}\text{S}_{0.11}$ were grown by the KCl/AlCl₃ chemical vapour transport method, as reported previously^{52,53}. More than 20 crystals were screened at ambient pressure and they showed sharp superconducting transition regions of ≈ 0.1 K, and large residual resistivity ratios up to 17 between room temperature and the onset of superconductivity. Crystals from the same batch were previously used in quantum oscillations and ARPES studies^{17,19}.

Magnetotransport measurements. High-magnetic-field measurements up to 45 T at ambient pressure and under hydrostatic pressure were performed using the hybrid magnet d.c. facility at the National High Magnetic Field Laboratory in Tallahassee, FL, USA. Pressures up to 17 kbar were generated using a NiCoCr piston cylinder cell, using Daphne Oil 7575 as pressure medium. The pressure inside the cell was determined by means of ruby fluorescence at low temperatures where quantum oscillations were observed. Different samples were measured simultaneously under pressure: sample B was used for transport measurements, and sample D-TDO was positioned inside a coil and the resonant frequency of an LC tank circuit driven by a tunnel diode was recorded (TDO). Transport sample E was measured at ambient pressure at the same time. Magnetotransport measurements were performed using the standard a.c. technique. Pulsed-field measurements up to 80 T at ambient pressure were carried out in Toulouse, using the same samples (transport measurements on sample B, TDO measurements on sample D). Magnetotransport and Hall effect measurements under pressure using a five-contact configuration were carried out on sample A in low fields up to 16 T in an Oxford Quantum Design Physical Property Measurement System and an ElectroLab High Pressure Cell, using Daphne Oil 7373, which ensures hydrostatic conditions up to about 23 kbar. The pressure inside this cell was determined via the superconducting transition temperature of Sn after cancelling the remanent field in the magnet. The magnetic field was applied along the crystallographic *c* axis for all samples. A maximum current of up to 2 mA flowing in the conducting tetragonal *ab* plane was used.

Resistivity power law. The temperature and pressure dependence of n is defined as $n = \partial \log(\rho - \rho_0) / \partial \log T$, with ρ_0 extrapolated from low temperatures. To extrapolate the zero-field resistivity at finite temperature, $\rho_0(T)$, in the absence of superconductivity (Supplementary Fig. 2), we perform a two-band model fit to the symmetrized magnetotransport data⁵⁴.

Estimate for T_{FL} . For a system with a strong nematic coupling, this interaction leads to an enhanced nematic transition temperature $T_c > T_0$, where T_0 is the bare transition temperature in its absence^{27,47}. Furthermore, below a crossover temperature T_{FL} , the coupling quenches the critical modes to small

regions in *k*-space, which will lead to Fermi liquid behaviour. To estimate the scale of T_{FL} , it is expected that the nematic quantum critical point is shifted to a larger tuning parameter $r_0 > 0$ caused by the nematicoelastic coupling²⁷. This shift is linearly related to T_s and T_0 as $r_0 \approx k_B(T_s - T_0)/E_F$, where E_F is the Fermi energy and k_B is the Boltzmann constant. The value of T_0 can be estimated from electronic Raman scattering²⁷ or elastoresistivity measurements²¹. For FeSe, $T_0 \approx 30$ K from electronic Raman scattering⁵⁵ and $T_0 \approx 34$ K from elastoresistivity measurements²¹. For $\text{FeSe}_{0.89}\text{S}_{0.11}$, we use the ambient pressure values $T_0 = 15$ K and $T_s = 60$ K (see also Supplementary Fig. 1) and a Fermi energy of $E_F \approx 50$ meV (ref.¹⁸). We thus obtain $r_0 \approx 0.077 \ll 1$, comparable to estimates for other iron-based superconductors²⁷. From this, we can determine T_{FL} using $T_{\text{FL}} \approx r_0^{3/2} E_F / k_B$ (ref.²⁷). We find that $T_{\text{FL}} \approx 13$ K for $\text{FeSe}_{0.89}\text{S}_{0.11}$. This value is well within the experimentally accessible temperature range and it is consistent with the crossover region of the resistivity exponent n at T_{FL} , shown in Fig. 1b (also Supplementary Fig. 1D).

Quantum oscillations. To quantify the complex oscillatory spectra of quantum oscillations, we use a fast Fourier transform (after removing a smooth and monotonic polynomial background from the raw data) or directly fit the Lifshitz-Kosevich formalism to the raw data in field (with a low-pass filter applied), as shown in Fig. 2c and Supplementary Figs. 4 and 6. The frequencies of the quantum oscillations are related to the extremal areas on the Fermi surface normal to the applied magnetic field, A_k , via the Onsager relation, $F = A_k h / (2\pi e)$ (ref.³⁹).

Data availability

The experimental data in our manuscript are available through the ORA depository at the University of Oxford at <https://doi.org/10.5287/bodleian:2REyEPKZX>. Other information is available from the corresponding authors upon reasonable request.

References

52. Böhmer, A. E. et al. Lack of coupling between superconductivity and orthorhombic distortion in stoichiometric single-crystalline FeSe. *Phys. Rev. B* **87**, 180505 (2013).
53. Böhmer, A. E., Taufour, V., Straszheim, W. E., Wolf, T. & Canfield, P. C. Variation of transition temperatures and residual resistivity ratio in vapor-grown FeSe. *Phys. Rev. B* **94**, 024526 (2016).
54. Proust, C., Vignolle, B., Levallois, J., Adachi, S. & Hussey, N. E. Fermi liquid behavior of the in-plane resistivity in the pseudogap state of $\text{YBa}_2\text{Cu}_3\text{O}_8$. *Proc. Natl Acad. Sci. USA* **113**, 13654–13659 (2016).
55. Massat, P. et al. Charge-induced nematicity in FeSe. *Proc. Natl Acad. Sci. USA* **113**, 9177–9181 (2016).